

## DYNAMICAL OUTCOMES OF PLANET–PLANET SCATTERING

SOURAV CHATTERJEE,<sup>1</sup> ERIC B. FORD,<sup>2,3</sup> AND FREDERIC A. RASIO<sup>1</sup>

<sup>1</sup> Department of Physics and Astronomy, Northwestern University, Evanston, IL 60208, USA  
<sup>2</sup> Harvard-Smithsonian Center for Astrophysics, Mail Stop 51, 60 Garden Street, Cambridge, MA 02138, USA and  
<sup>3</sup> Hubble Fellow

*Draft version May 27, 2019*

### ABSTRACT

Observations in the past decade have revealed extrasolar planets with a wide range of semi-major axes and eccentricities. Based on the present understanding of planet formation via core accretion and oligarchic growth, we expect that giant planets often form in closely packed configurations. While the protoplanets are embedded in a protoplanetary nebula, dissipation prevents eccentricity growth and can suppress instabilities from becoming manifest. However, once the disk dissipates, eccentricities can grow rapidly, leading to close encounters between the planets. In this study we explore strong gravitational scattering in a gas-free multi-planet system as a mechanism to explain the orbital properties of exoplanets. We numerically investigate the long-term stability of representative multi-planet systems containing three giant planets in orbit around a solar-like central star. We assign the planet masses in a realistic manner following the core accretion scenario of planet formation. In contrast to the case of two planets, there is no sharp stability boundary for 3-planet systems, so numerical integrations of 3-planet systems can approach instability naturally, even without including dissipation, mass growth, or migration. We characterize the timescale to reach instability as a function of the initial planet–planet separation. We discuss strong gravitational scattering as a possible mechanism to create high eccentricities as well as the close-in planetary orbits in the observed exoplanet population. We find that this mechanism can reasonably reproduce the observed eccentricity distribution. Our results also make testable predictions for the inclinations of short-period giant planets that are formed via strong planet scattering followed by tidal circularization.

*Subject headings:*

### 1. INTRODUCTION

The study of extrasolar planets and their properties has become a very exciting area of research over the past decade. Since the detection of the planet 51 Peg b, more than 200 new planets (Butler et al. 2006, see also <http://exoplanet.eu/>) have been detected and the large sky surveys planned for the near future can potentially detect many more. These detections have raised many questions about the formation and dynamical evolution of planetary systems. The extrasolar planet population covers a much greater portion of the semi-major axis and eccentricity plane than was expected based on the planets in our solar system (Lissauer 1995, Figure 1). The highly eccentric orbits and the presence of many giant planets in very short-period orbits (the “hot Jupiters”) are particularly puzzling.

Different scenarios have been proposed to explain the high eccentricities. The presence of a distant companion in a highly inclined orbit can increase the eccentricities of the planets around a star through Kozai oscillations (Mazeh et al. 1997; Holman et al. 1997). However, this alone cannot explain the observed eccentricity distribution (Takeda & Rasio 2005). Interaction with the protoplanetary gas disk could either excite or damp the eccentricities depending on the properties of the disk and the orbits. However, the combined effects typically result in eccentricity damping (Tremaine & Zakamska 2004, and references therein). Migration of two planets and trapping in a mean motion resonance (MMR) can also pump up the eccentricities efficiently, but this

mechanism requires strong damping at the end or termination of migration right after trapping in resonance (Lee & Peale 2002). Zakamska & Tremaine (2004) proposed inward propagation of eccentricity after the outer planets are excited to high eccentricities following a close encounter with a passing star. Using typical values for such interactions with field stars in the solar neighborhood, however, they do not get very high eccentricities. Papaloizou & Terquem (2001); Terquem & Papaloizou (2002); Black (1997) propose a very different formation scenario for planets from protostellar collapse in which both hot Jupiters and eccentric planets at higher semi-major axes are formed naturally. This scenario, however, cannot form sub-Jupiter-mass planets.

In this paper, we explore another promising way to create high eccentricities: strong gravitational scattering between planets in a multi-planet system undergoing dynamical instability (Rasio & Ford 1996; Weidenschilling & Marzari 1996; Lin & Ida 1997). According to the model of oligarchic growth, planetesimals form in a nearly maximally packed configuration in the protoplanetary disk (Goldreich et al. 2004; Ida & Lin 2004b; Kokubo & Ida 2002). Once the disk dissipates, mutual planetary perturbations (“viscous stirring”) of the planetesimals will lead to eccentricity growth, orbit crossing, and eventually close encounters between the big bodies in the disk (Ford & Chiang 2007; Levinson & Morbidelli 2007). While planetary systems with more than two planets can not be provably stable, they can remain stable for very long timescales depending on their initial separations (Chambers et al. 1996;

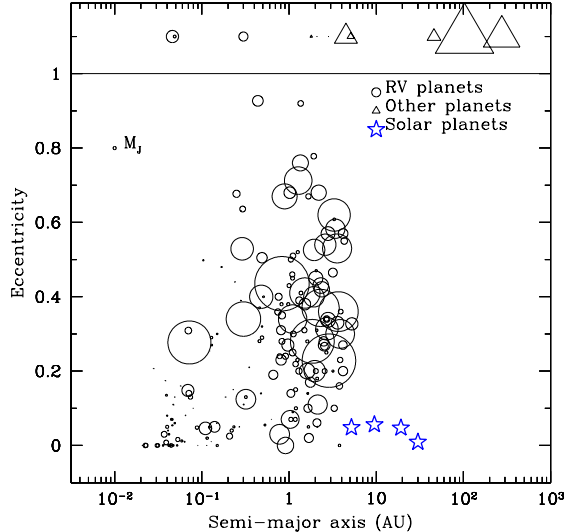


FIG. 1.— Semi-major axis vs eccentricity plot for the detected planets. The sizes of the points are proportional to the minimum masses ( $m \sin i$ ) of the corresponding planets. The size of a Jupiter mass planet is shown at the left top corner for reference. The stars represent the four giant planets in our solar system (for these the sizes do not indicate their mass). The open circles show the planets detected by radial velocity surveys. The triangles show planets detected by micro-lensing or direct imaging. Planets with poorly constrained eccentricities are plotted above  $e = 1$ . A horizontal line is drawn at  $e = 1$  to guide the eye. Note the logarithmic scale of the semi-major axis.

Marzari & Weidenschilling 2002). A sufficiently massive disk can prevent interacting planets from acquiring large eccentricities and developing crossing orbits. However, once the disk is sufficiently depleted, the eccentricities of the planets can grow to high values, possibly leading to strong planet–planet scattering and a phase of chaotic evolution that dramatically alters the orbital structure of the system.

The detection of close-in planets with orbital periods as short as  $\sim 1$  d, the so-called hot Jupiters (and, more recently, hot Neptunes and super-Earths), was another major surprise. Giant planets are most likely to form at much larger separations, beyond the ice line of the star where there can be enhanced dust production (Kokubo & Ida 1998, 2002; Ida & Lin 2004b). It is widely believed that the giant planets form beyond the ice line and then migrate inwards to form the hot Jupiters we observe today. Different kinds of inward migration scenarios have been proposed to explain the hot Jupiters, but it is unclear why they pile up at just a few solar radii around the star, rather than keep migrating and eventually accrete onto the star.

Strong gravitational scattering between planets in a multi-planet system may provide another way to create these close-in planets (Rasio & Ford 1996). A few of the planets scattered into very highly eccentric orbits could have sufficiently small periastron distances that tidal circularization takes place, giving rise to the hot Jupiters. The currently observed edge in the mass-period diagram is very nearly at the ideal circularization radius (twice the Roche limit), providing support for this model (Ford & Rasio 2006). Faber et al. (2005) finds that these violent passages might not destroy the planets completely even if mass loss occurs.

In previous work, numerical simulations were done to explore strong gravitational scattering with two giant planets around a solar-like star (Rasio & Ford 1996; Ford et al. 2001). The conclusion was that the observed eccentricity distribution is not easily produced in systems with two equal-mass planets. However, Ford et al. (2003) and Ford & Rasio (2007) show that strong scattering of two *unequal* mass planets could explain the observed eccentricities of most extrasolar planets. A system with three (or more) giant planets of comparable masses is qualitatively different than a two-planet system, since there is no sharp stability boundary in the 3-planet case (Chambers et al. 1996). Therefore, simulations of 3-planet systems can very naturally approach instability and may be more representative of how such instabilities arise in real systems. Chambers et al. (1996) has studied systems with 3 planetesimals around a central star, but their small masses prevented ejections, which are essential for generating large eccentricities. Marzari & Weidenschilling (2002) (hereafter MW02) have previously performed simulations of unstable systems with three giant planets around a solar-like star, but their results are limited by the relatively small number of systems with different initial conditions that they have examined. In this paper we explore the outcomes of strong planet–planet scattering in more realistic systems containing three giant planets around a solar mass star. In particular, our model systems are more realistic in their initial distribution of planetary masses (cf. Sec. 3.1). We also introduce modest inclinations to the initial planetary orbits to study possible inclination dependent effects. In Sec. 2 we present a timescale study for the onset of instability in these systems. In this section, we closely follow the treatment in MW02 for easy comparison. In Sec. 3 we explore the final orbital properties for two sets of more realistic initial conditions. We summarize and conclude in Sec. 4.

## 2. STABILITY TIMESCALES

According to the core accretion model of planet formation, planets form in a protoplanetary disk separated by a small number of Hill radii away from each other (Kokubo & Ida 1998, 2002). The timescale for the onset of instability depends on the planet–planet separations measured in terms of the mutual Hill radii. In this section we first perform a timescale study similar to the one in MW02, but using a finer sampling and many more runs to produce better statistics. As described below, we also use more general initial inclinations for the planetary orbits.

### 2.1. Numerical setup

For this timescale study we idealize the system in the following way. We integrate three identical Jupiter mass ( $M_J$ ) planets orbiting around a central star of  $1 M_\odot$  at distances of several AU. The planets interact with each other through gravity and physical collisions only. In this section we do not use a realistic mass distribution for the planets (cf. Sec. 3.1) in order to provide a more direct comparison with MW02. We assume that the disk is completely depleted from the system. We use the MERCURY6.2 software for all our integrations (Chambers 1999). For this part we use the mixed variable symplectic

integrator with 200-day timesteps. We stop the integration after the first close encounter and record the time, which we define to be the timescale of instability for the solar system. Two planets approaching within one Hill radius defines a close encounter in this case.

Following the prescription in MW02, we put the planet closest to the star at 5 AU and then determine the semi-major axes of the other two planets as follows,

$$a_{i+1} = a_i + K R_{H,i,i+1}, \quad (1)$$

where  $K$  is the spacing measured in terms of  $R_{H,i,i+1}$ , the mutual Hill radius for the  $i^{th}$  and  $i+1^{th}$  planets,

$$R_{H,i,i+1} = \left( \frac{M_i + M_{i+1}}{3M_*} \right)^{1/3} \frac{a_i + a_{i+1}}{2}. \quad (2)$$

Here  $M_i$  is the mass of the  $i^{th}$  planet,  $M_*$  the mass of the central star, and  $a_i$  the semi-major axis of the  $i^{th}$  planet.

We integrate a number of 3-planet systems with different initial conditions: 1000 for  $K \leq 4.3$ , 500 for  $4.3 < K \leq 5.0$  and 200 for  $K \geq 5.0$ . The initial eccentricities of the planets are drawn from a uniform distribution between 0 to 0.1. We choose the inclinations of the orbits randomly between  $0^\circ$  to  $10^\circ$  with respect to the orbital plane of the closest planet. All the other angles describing the orbits are chosen randomly in the full range.

## 2.2. Results

After integrating a number of systems as described above we calculate the distribution of the instability onset timescales. Figure 2 shows the results as a function of  $K$ . The filled circles show the median and the bars above and below represent  $\pm 34\%$  around the median. We also show the mean of each distribution to compare it with the median. In each case the mean overestimates the timescale and lies often outside the 34% bars around the median.

As in MW02 we find that the timescale to instability increases rapidly as  $K$  increases. Low-order MMRs leave their signatures in dips or rises of the timescale. For each of these major resonances, the median timescale for instability dips for close but slightly lower  $K$  values, whereas, at the resonance  $K$  values the median is higher. For example, the prominent drop in stability timescale between  $K = 4.8 - 5$  corresponds to a 2 : 1 resonance between the 1<sup>st</sup> and 2<sup>nd</sup> as well as the 2<sup>nd</sup> and 3<sup>rd</sup> planets at  $K = 5.1$ . The drop at  $K = 3$  and the rise in the range  $K = 3.1 - 3.4$  are due to the proximity of the 3 : 2 MMR between the 1<sup>st</sup> and 2<sup>nd</sup> as well as the 2<sup>nd</sup> and 3<sup>rd</sup> planets situated at  $K = 3.1$ . Another possible MMR is between  $K = 4.1$  and 4.2 due to 3 : 1 commensurability between the 3<sup>rd</sup> and the 1<sup>st</sup> planetary periods. However, we do not see any strong effect of that particular MMR on the instability growth timescales. For systems with initial conditions close to but not exactly at MMR, a few lucky ones might obtain the right initial phases leading to a stable MMR. However, all others will become more unstable, which is seen in the prominent dips in the median timescales. We also note that these resonances affect the timescales in a wide range of  $K$  values around the ex-

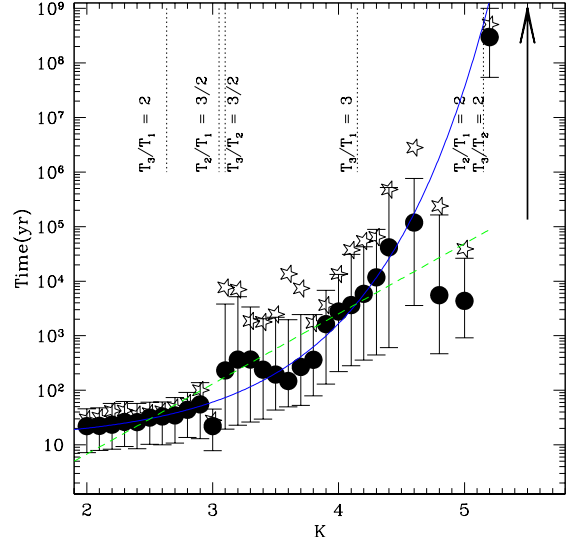


FIG. 2.— Instability growth timescale as a function of spacing parameter  $K$ . The filled circles are the medians of the distributions of stability timescales for the respective values of  $K$ . The bars show the  $\pm 34\%$  range in the timescale. Note that they are not error bars, instead they represent the distribution of the stability timescales. The medians are shown in the plot because the distributions are skewed towards greater timescales. The open stars show the mean of the timescale distribution. Signatures of some major resonances can be noticed in the sudden dips in timescale. The starting point of the arrow indicates that most systems with  $K = 5.5$  are stable for at least  $10^9$  years. The starting point of the arrow represents the shortest instability timescale among our simulations. The solid line (blue) and the dashed line (green) show the empirical best fit lines predicting the medians of the stability timescale distributions given the  $K$  values (Eqs. 3, 4).

TABLE 1  
FIT:  $t$  vs  $K$

	a	b	c	Max Error(%)
Fit 1	1.07	0.03	1.10	10
Fit 2	-1.74	1.29		50

<sup>a</sup> The best fit values of the fitting parameters for the empirical fits for the median stability timescale of the systems as a function of their initial spacing parameter  $K$ .

act value corresponding to integral period ratios. This confirms the findings in MW02.

We found a simple empirical fitting formula for the median timescale to instability away from MMR. It can be expressed as a function  $t_m(K)$  of the spacing parameter  $K$ ,

$$\log_{10} t_m(K) = a + b \times \exp(cK), \quad (3)$$

where  $a$ ,  $b$ , and  $c$  are constants (henceforth, called Fit-1). The best fit values for  $a$ ,  $b$ , and  $c$  (Table 1) can predict the median timescales with fractional error less than 10% away from MMR. We also tried to find a simpler linear fit  $t_{m,linear}(K)$  for our data away from MMR, following MW02, writing

$$\log_{10} t_{m,linear}(K) = a + bK, \quad (4)$$

where  $a$  and  $b$  are fitting parameters (henceforth, called Fit-2). The best fit values for  $a$  and  $b$  are also given in Table 1. We find that Fit-1 is much better than Fit-2.

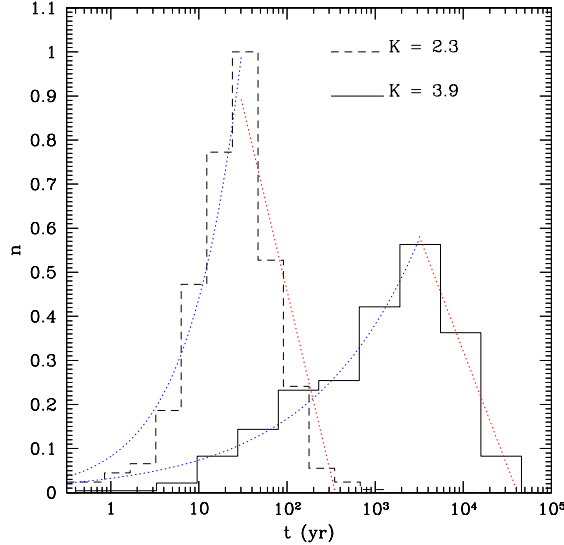


FIG. 3.— Histograms for the timescale distributions at two different  $K$  values both away from MMR. Note that times are shown in log scale. Each histogram shown here corresponds to  $10^3$  runs for that  $K$  value. The number distributions are normalized such that  $\sum_i n_i \Delta t_i = 1$ , where,  $\Delta t_i$  is the binsize in logarithm of time. This normalization essentially makes the area under each histogram normalized to 1. The solid histogram corresponds to  $K = 3.9$  and the dashed histogram corresponds to  $K = 2.3$ . Both these  $K$  values are away from any major MMR. The two histograms have essentially the same shape. The dotted (blue and red) curves show the analytical fitting curves for timescale distributions at the left and the right sides of the mode of the distributions. For systems with stability timescales less than the median of the distribution show an exponential shape, whereas, those with timescales higher than the median show a linear drop-off (see Eqs. 5, 6 and Table 2).

We note that the shapes of the distributions of the timescales are essentially the same for any  $K$  value away from a major MMR. In order to illustrate this fact we show the timescale distributions at two different  $K$  values, 2.3 and 3.9, both away from resonance (Figure 3). We find simple empirical fitting formulae to predict the distributions of the stability timescales. Note that the histograms of the timescale distributions are normalized such that  $\sum_i n_i \Delta t_i = 1$ , where,  $\Delta t_i$  is the bin size in logarithm of time. The normalized number distribution for times lower than the median timescale (henceforth denoted as  $n_L$ ) has an exponential shape, whereas, that above the median timescale (henceforth denoted as  $n_R$ ) has a linear decay for all  $K$  away from major MMRs. The fitting formulae for  $n_L$  and  $n_R$  are given by

$$n_L = N_L \exp [(\log_{10} t - \log_{10} t_m(K))/t_L], \quad (5)$$

$$n_R = N_R - t_R \log_{10} t. \quad (6)$$

For a given  $K$  value, the median timescale can be obtained using Eq. 3 and then using the median timescale the shapes of the distributions can be obtained using Eqs. 5 and 6. Here,  $N_{L,R}$  are the normalization constants for the peak amplitudes of the distributions,  $t_m(K)$  is the median of the timescale distribution as a function of  $K$ ,  $t_L$  and  $t_R$  are fitting constants characterizing the exponential index and the slope of the two curves, respectively. The best-fit values for  $N_{L,R}$ , and  $t_{L,R}$  are listed in Table 2.

The shapes of the normalized distributions for the timescales can be quite different depending on whether

TABLE 2  
FIT: TIMESCALE DISTRIBUTION  
( $n_{L,R}$ )

$K$	$t_L$	$N_L$	$t_R$	$N_R$
2.0	0.719	0.714	1.728	3.716
2.1	0.669	0.775	1.138	2.649
2.2	0.582	0.886	0.778	1.971
2.3	0.595	0.864	0.836	2.129
2.4	0.663	0.867	1.193	2.816
2.5	0.530	0.996	1.559	3.628
2.6	0.482	1.153	1.286	3.065
2.7	0.589	1.004	1.112	2.806
2.8	0.582	1.002	1.167	3.01
2.9	0.713	0.800	0.584	1.791
3.0	0.624	1.715	1.412	3.141
3.1	0.810	0.512	0.095	0.522
3.2	2.343	0.206	0.082	0.484
3.3	1.447	0.283	0.203	0.968
3.4	1.051	0.462	0.188	0.889
3.5	0.533	1.238	0.180	0.869
3.6	0.395	3.700	0.201	0.929
3.7	0.811	0.937	0.143	0.753
3.8	0.744	1.085	0.245	1.140
3.9	1.211	0.415	0.522	2.409
4.0	1.488	0.353	0.349	1.811
4.1	1.399	0.379	0.160	0.975
4.3	1.684	0.346	0.204	1.292
4.4	2.650	0.218	0.127	0.953
4.8	1.066	4.910	0.102	0.710
5.0	0.767	73.831	0.209	1.242

<sup>a</sup> Best fit values for the fitting parameters,  $N_L$ ,  $t_L$ ,  $N_R$ , and  $t_R$  predicting  $n_L$  and  $n_R$  for a given  $K$  and the median of the stability timescale distribution  $t_m(K)$ .

they are near or away from MMR. One example is shown in Figure 4, where two such distributions are shown, for two  $K$  values, one near and the other away from MMR.

### 3. MORE REALISTIC SYSTEMS

#### 3.1. Numerical setup

In an effort to represent more realistic initial conditions, we integrate 3 planets around a central star as described in section 2.1, but allowing for unequal masses of the planets. We mimic the core accretion scenario for giant planet formation in the following way. Planet masses depend on the distance of the planet from the central star through the dependence of the gas surface density in the protoplanetary disk. To assign the masses of the planets we closely follow the planet formation model described in Kokubo & Ida (2002, hereafter KI02). First, we assign the planetary core masses  $M_{core}$  uniformly between  $1 - 10 M_{\oplus}$ . Then, we assume that the cores accrete all the gas within 10 Hill radii (KI02) to reach a total mass of  $M$  at a semi-major axis  $a$  and a core mass  $M_{core}$ . Then  $M$  is given by

$$M = 2\pi a \Delta \Sigma_{gas} + M_{core}, \quad (7)$$

where  $\Delta = 10r_H$  is the feeding zone of the planet core and  $r_H$  is the Hill radius of the planet core, given by

$$r_H = \left( \frac{2}{3} \frac{M_{core}}{M_*} \right)^{1/3} a. \quad (8)$$

Here  $M_*$  is the mass of the central star and  $a$  is the distance of the core from the central star;  $\Sigma_{gas}$  is the gas

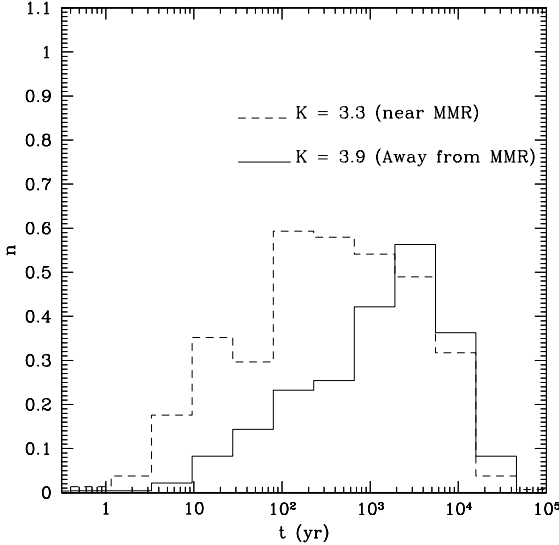


FIG. 4.— Histograms for the timescale distributions near and away from an MMR. Each histogram corresponds to  $10^3$  runs for that  $K$  value. We follow the same normalization scheme as mentioned earlier.  $K = 3.3$  is near the  $K$  value for a  $3:2$  commensurability between the periods of the first and the second as well as the second and the third planetary orbits (dashed line).  $K = 3.9$  is away from MMR (solid line). The distributions near and away from MMR have somewhat similar shapes for times lower than the medians of the distributions. However, for times higher than the medians the decay is not as sharp near a MMR as for systems far from a MMR.

surface density in the disk and is given by

$$\Sigma_{gas} = 240 \Sigma_1 \left( \frac{a}{1 \text{AU}} \right)^{-\frac{3}{2}} \text{g cm}^{-2}, \quad (9)$$

where the coefficient 240 is the assumed gas to dust ratio factor (taken from KI02),  $\Sigma_1$  is the surface density at 1 AU, and the exponent comes from the minimum mass disk model. We use  $\Sigma_1 = 10$  in this case which is a little higher than the minimum-mass Solar nebula value of 7. The choice of  $\Sigma_1$  is somewhat arbitrary and motivated to produce close to Jupiter-mass planets. The initial masses of the planets obtained with this procedure are between  $0.4 M_J - 1.2 M_J$ . Throughout this study we have assumed Jupiter's density ( $1.33 \text{ g cm}^{-3}$ ) as the density of all planets in our simulations to determine each planet's radius.

The initial eccentricities are drawn from a uniform distribution between 0—0.1, and the orbital inclinations are drawn from a uniform distribution between  $0^\circ$ — $10^\circ$  with respect to the initial orbital plane of the planet initially closest to the star. To find inclination dependent effects more easily we employ little higher range of inclinations than our Solar system planetary orbits. However, we do not extend it too much. We discuss in Sec. 3.3 why we expect and also verify numerically that this choice of initial inclination values do not affect the final inclination values significantly. The initial semi-major axis of the closest planet is 3AU, the other two planets are placed with the spacing law

$$a_{i+1} = a_i + 3.5 R_{H,i}, \quad (10)$$

where  $R_{H,i}$  is the Hill radius of the  $i^{\text{th}}$  planet. The choice of the initial semi-major axis of the initially closest planet and the value of  $K = 3.5$  are somewhat arbitrary, but are

guided by the following constraints. We choose systems where close encounters happen rather quickly, so that we can integrate after the chaotic stage is over for most of the systems. Also we make sure that initially the systems are not in a MMR. Both conditions can be satisfied easily by choosing a suitable  $K$  value, which determines the initial spacing between the planet orbits in terms of their Hill radii (Figure 2). The initial phase angles are assigned random values between  $0^\circ$ — $360^\circ$ .

We integrate each system for  $10^7$  years, which is  $2 \times 10^6$  times the initially closest planet's period ( $T_{1,i}$ ), and also  $\sim 10^5$  times the instability onset timescale for the given initial conditions. We integrate the systems symplectically when there is no close encounter with a timestep of 10 days and switch to Bulirsch-Stoer (BS) as soon as two planets have a close approach (closer than 3 Hill radii) using the hybrid integrator of MERCURY6.2 (Chambers 1999). Runs with poor energy conservation ( $|dE/E| \geq 0.001$ ) with the hybrid integrator are repeated with the BS integrator. This happens in  $\sim 30\%$  of the total number of runs. We integrate  $10^3$  systems with different initial conditions and present the results statistically. We find that for all systems at least one planet is ejected eventually. For systems with two remaining planets we check for Hill stability using the known semi-analytic criteria (Gladman 1993). In our simulations about 9% of systems were not provably stable at the integration stopping time. We discard those from our analysis. We treat collisions in the following simple way (“sticky-sphere” approximation). Collisions are assumed to happen when the distance between two planets is less than the sum of their physical radii. When two planets collide they stick together creating a single planet of mass equal to the sum of the masses of the colliding planets. The dynamical properties of the merger product are then determined using conservation of momentum. We find that collisions are not important with the given initial conditions, so it is possible to present our results in a scale-free manner where all lengths are given in units of the initial semi-major axis of the initially closest planet ( $a_{1,i}$ ) and all times in units of the initial inner planet's orbital period ( $T_{i,1}$ ).

Two representative time-evolution plots are shown in Figure 5 and Figure 6. Figure 5 represents a system with two planets remaining in a stable configuration. In this particular system the initially closest planet has multiple orbit crossing episodes with the other two planets before eventually getting ejected at  $4.1 \times 10^4 T_{1,i}$ . The top panel shows the time-evolution of the semi-major axes of the three planets. After the ejection of the inner planet the other two planets become stable. The bottom panel shows the eccentricity evolution of the planets. Note the clear chaotic eccentricity evolution of the planets until the ejection happens, after which the eccentricities of the remaining bound planets go through stable secular oscillations.

Figure 6 represents a case where the initially closest planet collides and merges with the initially furthest planet at  $\sim 4.5 \times 10^3 T_{1,i}$ . Then at  $\sim 7 \times 10^4 T_{1,i}$  the initial middle planet gets ejected. We stop integration when there is only one remaining planet bound to the central star since the configuration is always stable. Note the orbit crossing episodes in the top panel and the cor-

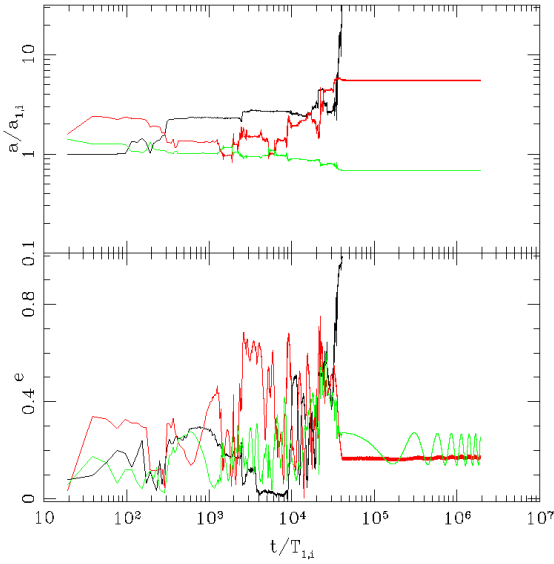


FIG. 5.— Time evolution of the semi-major axes (top panel) and the eccentricities (bottom panel) of a typical simulation. The black, red and green lines show the orbital elements for the initially closest ( $a_1, e_1$ ), middle ( $a_2, e_2$ ) and the furthest ( $a_3, e_3$ ) planets. In this particular integration, the first planet is ejected at  $\sim 4.1 \times 10^4 T_{1,i}$ , and the integration concludes with two planets in provably stable orbits. The semi-major axes for both  $P_2$  and  $P_3$  remain constant and the eccentricities oscillate stably on a secular timescale. Numbers in the subscript represent the positional sequence of the planets starting from the star and letters “i” and “f” mean initial and final values, respectively. We employ the same convention in all our plots.

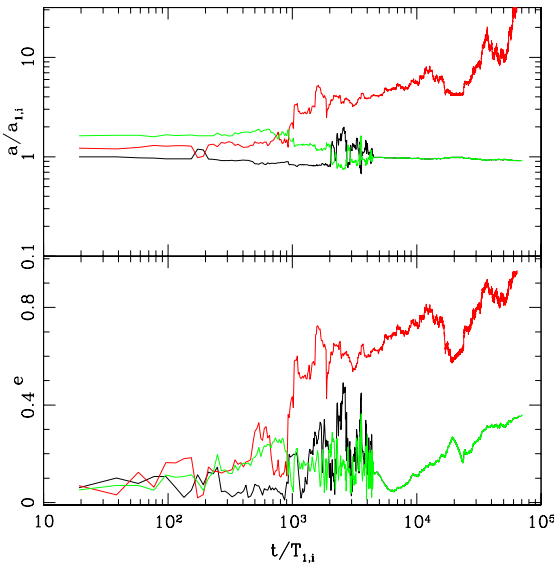


FIG. 6.— Same as Figure 5, but for a simulation that concludes with a single planet orbiting the central star. The initial closest planet merges with the initial furthest planet through collision at  $\sim 4.5 \times 10^3 T_{1,i}$ . Then at  $\sim 7 \times 10^4 T_{1,i}$  the initial middle planet gets ejected. We stop integration after that since a single planet around a central star is stable and will maintain a constant semi-major axis and eccentricity.

responding chaotic eccentricity changes.

### 3.2. High eccentricities and hot Jupiters

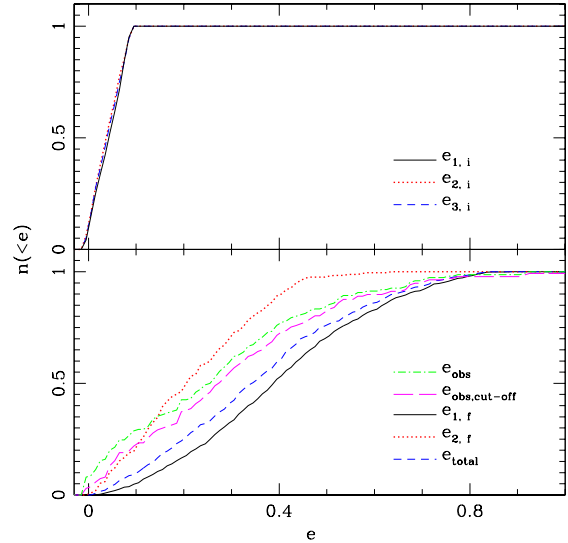


FIG. 7.— Cumulative distributions showing initial and final eccentricities of the planets. Top and bottom panels show the initial and final cumulative eccentricity distributions, respectively. In the top panel solid (black), dotted (red) and dashed (blue) lines represent the closest, middle, and furthest planets, respectively. They are on top of each other because the initial eccentricity distribution is the same for all of the planets. In the bottom panel solid (black) and dotted (red) lines represent the final inner planets. The dotted (red) line shows the outer planets with semi-major axes  $< 10$  AU. The dashed (blue) line shows all planets, both inner and outer within 10 AU from the central star. The semi-major axis cut-off is used to compare the simulated population with the observed population more easily. For comparison, the dash-dot line (green) in the bottom panel shows the eccentricity distribution of the observed giant planets with a mass cut-off of  $0.4 M_J$ , since we do not have planets less massive than that in our simulated population. The dashed line with longer dashes (magenta) represents the eccentricity distribution of the observed exoplanets more massive than  $0.4 M_J$  and semi-major axes greater than  $0.03 a_{1,i}$ .

We find that strong scattering between planets increases the eccentricities very efficiently (Figure 7). The median in the eccentricity distribution for the final inner planets is 0.38. The median eccentricity for the final outer planets with semi-major axes  $< 10$  AU is at 0.28 whereas the median for all simulated planets is at 0.33. We compare our results with the observed eccentricity distribution of the detected extrasolar planets (Fig. 7). For that we use a lower mass cut-off of  $0.4 M_J$  following the lower mass cut-off of our simulated population. To show how the eccentricity distribution of the observed exoplanet population changes with imposed lower semi-major axis cut-off we also plot the same but now using only exoplanets with semi-major axes  $> 0.03 a_{1,i}$ . The upper semi-major axis cut-off (10 AU) for the simulated final planet population is used to address the fact that we cannot observe planets further out from the central star.

As seen in the figure we seem to overestimate the eccentricities of the inner planet. However, the slopes of the cumulative eccentricity distributions at higher eccentricity values are similar. In a realistic planetary system, there can be damping effects of lingering gas, dust or planetesimals in a protoplanetary disk. Both of the above will lower the eccentricities of the planets in a real planetary system. While our simplistic simulations come reasonably close to matching the eccentricity distribution

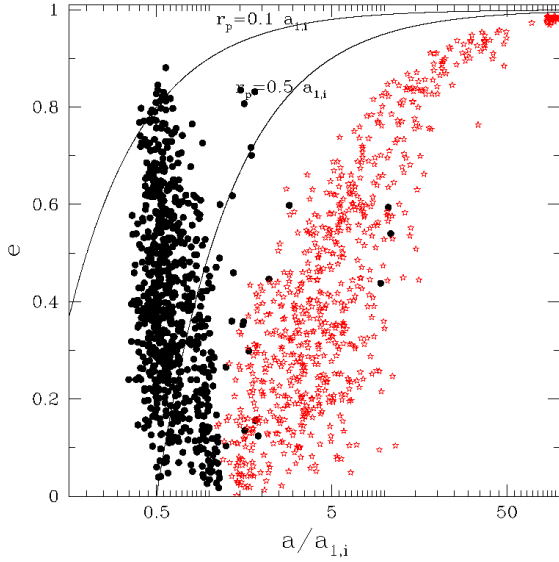


FIG. 8.— Final semi-major axis versus eccentricity plot. All lengths are scaled by the initial closest planet semi-major axis (here  $a_{1,i} = 3.0\text{AU}$ ). Black solid circles and red open stars represent the final inner and outer planets, respectively. Solid lines show different constant periape distances with values 0.1 and 0.5. Note the high eccentricities and the close approaches towards the central star. The empty wedge shaped region in the  $a$ - $e$  plane at high eccentricities is due to the requirement for orbital stability.

of observed planets, including damping might improve the eccentricity distribution. In Sec. 3.5 we show that a slightly different initial distribution of planet masses results in a very good match to the eccentricity distribution for  $e > 0.25$ , without any dissipation.

We find a significant fraction of systems with planets in orbits that can take them to small periape distances to the star. Figure 8 shows the final positions of the planets that are still bound to the central star in the  $a$ - $e$  plane. The solid lines represent different constant pericenter distances labeled near the corresponding lines in the figure. Note that the planets show weak correlations between the eccentricity and the semi-major axis. For the inner planet, planets with lower semi-major axes tend to have higher eccentricities, whereas the outer planets show an opposite trend. The final inner and outer planets make two clearly separated clusters of points in the  $a$ - $e$  plane due to stability considerations.

Figure 9 shows the cumulative distribution of the periastron distances of the final bound planets around the star. For the sake of comparison, we also show the pericenter distribution of the observed exoplanet population in Figure 9. 10% of the systems harbor planets with periape distances  $\leq 0.1a_{1,i}$ . If the initial semi-major axes are sufficiently small then the planets can effectively have small periastron distances so that tidal forces between the star and the planet become important and a highly eccentric orbit can be circularized to produce a short-period giant planet (Ford & Rasio 2006; Faber et al. 2005). We caution that if similar systems had been started with much smaller  $a_{1,i}$  (and the same planetary radii), then collisions might become the most common final outcome.

### 3.3. Implications for Short-Period Planets

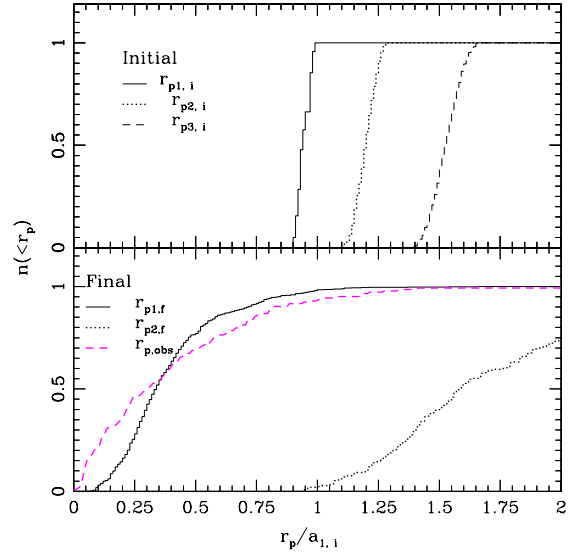


FIG. 9.— Cumulative histogram of the pericenter distance of the initial (top panel) and final (bottom panel) planets bound to the star. In the top panel the solid, dotted and dashed lines show the pericenter distributions of the initial closest, middle and the furthest planets, respectively. In the bottom panel the solid and dotted lines show the same for the final stable inner and the outer planets with their semi-major axes less than 10 AU. The dashed magenta line shows the pericenter distribution of the observed exoplanet population for comparison purposes. The length scaling used for the observed population is  $a_{1,i} = 2.5\text{ AU}$ .

The top and bottom panels in Figure 10 show the cumulative distributions of the initial and final semi-major axes for the planets respectively. The planet that is closest initially may not remain closest at the end due to the close encounters and orbit crossing. We find that in  $\simeq 1/3$  of the cases the initially closest planet remains the closer planet finally, in  $\simeq 1/3$  of the cases the initially middle planet ends up being the closer planet, and in the rest of the cases the initially furthest planet becomes the closer planet finally. Also 20% of the final stable systems have a single planet around the central star, two planets being lost from the system either through collisional merging or ejection.

We see a very interesting trend in the final orbital inclinations. Figure 11 compares the distributions of several inclinations. Here each inclination reported is the absolute value of the orbital inclinations measured with respect to the initial invariable plane. The initial invariable plane is defined as the plane perpendicular to the initial total angular momentum vector of the planetary orbits of the planetary system. Note that the initial “invariable plane” can differ since planets can be ejected from the system and carry away angular momentum.

The top panel shows the initial and final RMS inclinations. Clearly strong scattering between planets increases inclinations of the orbits leading to higher final RMS inclination as can be seen in the top panel of Figure 11. The middle and bottom panels in Figure 11 show the initial and the final inclinations of the orbits of the individual planets. In general, the inclinations tend to increase for each planet. Additionally, we note that the inclination of the final inner planet statistically has larger values (bottom panel, Figure 11) than the outer. The relative inclinations between the remaining planet

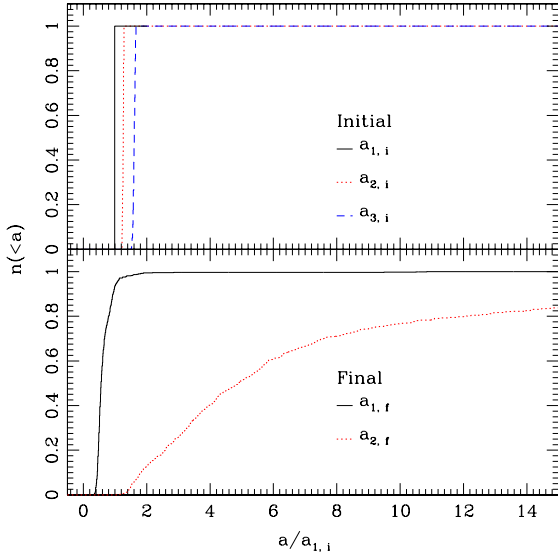


FIG. 10.— Cumulative frequency plots of semi-major axes of the initial (top panel) and final (bottom panel) planets. Vertical solid (black), dotted (red) and dashed (blue) lines show the initial values in the top panel. These are vertical lines because the initial semi-major axes of the closest, middle and outer planets do not have a spread. Solid (black) and dotted (red) curves in the bottom panel show the final inner and outer planets' semi-major axes, respectively.

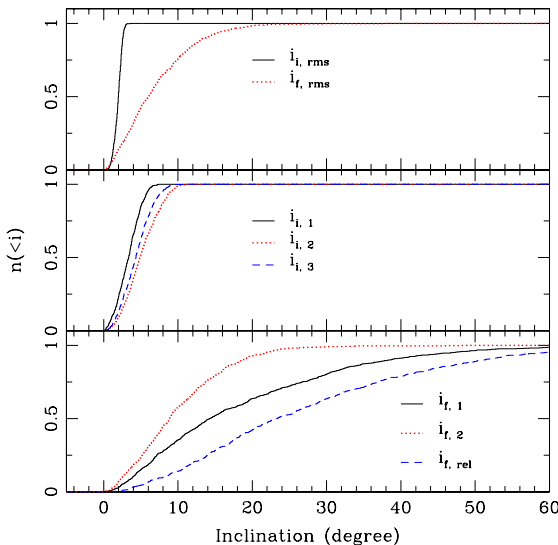


FIG. 11.— Cumulative distribution showing initial and final orbital inclinations of the planets with respect to the initial invariable plane. In the top panel the solid (black) and the dotted (red) lines represent the initial and final RMS inclination distributions of the planet orbits with respect to the initial invariable plane. In the middle panel solid (black), dotted (red) and dashed (blue) lines represent the closest, middle and furthest planets, respectively. The bottom panel shows the final orbital inclination distributions of the remaining planets in the system. The solid (black), and the dotted (red) lines represent the inner and outer planets, respectively. The dashed (blue) line represents the relative angles between the two remaining planetary orbits. Note that the final closer planets, which are the planets more easily observable in a planetary system, statistically have higher inclinations. Also note that the relative inclinations between the planetary orbits are also quite high.

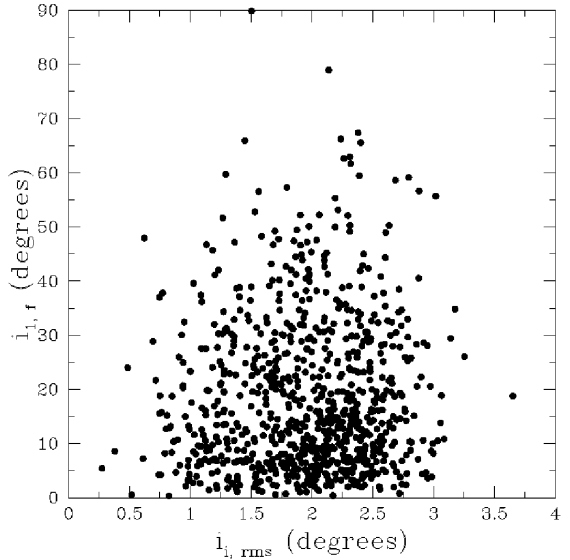


FIG. 12.— This figure shows the initial RMS inclination vs final inclination of the inner-most planet. Note that the final closer planet orbital inclination is largely insensitive to the initial RMS inclination.

orbits is also quite high (Figure 11, bottom panel).

If it is true that the timescale for tidal damping of inclinations is much greater than the age of the stars (Winn et al. 2005), then the significantly increased inclinations should be found in some planetary systems that have gone through strong gravitational scattering phases in their lifetimes. Since the star and the planets get their angular momenta from the same source, planetary orbits are expected to form in a coplanar disk perpendicular to the stellar spin axis. However, our results show that strong planet-planet scattering can dramatically affect the coplanarity of some planetary systems. Measuring a poor degree of alignment between the star spin axis and the planetary orbits could be used to recognize some systems that have undergone a tumultuous dynamical history.

We expect that the chaotic phases erase any substantial correlation between the initial and final properties. Here, we test this hypothesis by investigating the correlation between the initial and final inclinations. Of course if a system is initially assigned a strictly coplanar configuration, then the angular momentum conservation dictates the system to remain coplanar. However, apart from that trivial situation we find that the final inclination of the inner planet does not depend on the initial RMS inclination (Figure 12). We quantify the amount of correlation between the initial RMS and the final orbital inclination of the final inner planet using the bivariate correlation coefficient. The bivariate correlation coefficient ( $r_{xy}$ ) for two variables  $x$  and  $y$ , is given by the following equation.

$$r_{xy} = \frac{\text{Cov}(x, y)}{sd(x)sd(y)}, \quad (11)$$

where  $\text{Cov}(x, y)$  is the covariance of  $x$  and  $y$ , given by

$$\text{Cov}(x, y) = \frac{1}{n} \left( \sum_{i=1}^n (x_i - \bar{x})(y_i - \bar{y}) \right), \quad (12)$$

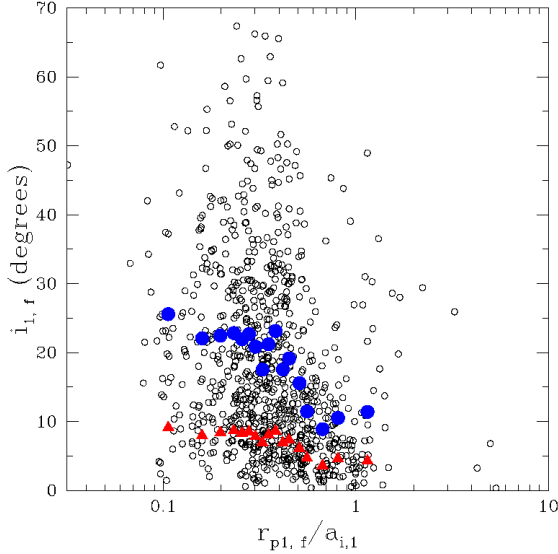


FIG. 13.— Pericenter distance vs inclination of the final inner planets. The open dots show the final positions of the final inner planet in the pericenter-inclination plane. The filled disks (blue) and triangles (red) represent the mean orbital inclination of the inner planet and the final RMS inclinations, respectively. The means are obtained for bins of equal population ( $n_{bin} = 50$ ). We observe a weak anti-correlation between the pericenter and the inclination.

and  $sd(x)$  or  $sd(y)$  is the standard deviation of  $x$  or  $y$  defined as follows.

$$sd(x) = \left( \frac{1}{n} \sum_{i=1}^n (x_i - \bar{x})^2 \right)^{1/2}. \quad (13)$$

We find that the correlation coefficient between the initial RMS and the final orbital inclinations is  $r_{iRMS,iclose} = 0.05$ . The low value of  $r$  bolsters the belief that the high final inclinations are not merely reflection of the initial orbital inclinations. Thus, as long as the planetary system is not strictly coplanar to begin with, strong planet–planet scattering can increase the orbital inclinations of some systems significantly.

The final inclination of the inner planet orbit, which is the most easily observable, shows a weak anti-correlation with the pericenter distance of the orbit (Figure 13); lower pericenter orbits tend to have higher inclinations. The correlation coefficient in this case is  $r_{rp,iclose} = -0.13$  using Eq. 11.

We look forward to future observations that determine the degree of alignment between the stellar spin and the planetary orbits. For our solar system, the angle between the spin axis and the invariable plane is  $\simeq 6^\circ$ . The angle between the stellar rotation axis and the orbital angular momentum of a transiting planet ( $\lambda$ ) can be constrained via the Rossiter-McLaughlin effect. Observations have measured  $\lambda \sin i$  for four systems (Winn 2006b):  $-4.4^\circ \pm 1.4^\circ$  for HD 209458b (Winn et al. 2005),  $-1.4^\circ \pm 1.1^\circ$  for HD 189733b (Winn et al. 2006),  $11^\circ \pm 15^\circ$  for HD 149026b (Wolf et al. 2007), and  $0^\circ \pm 30^\circ$  for TrES-1b (Narita 2006). Our study implies that planetary systems with a tumultuous dynamical history will sometimes show a large  $\lambda$ . Therefore, we look forward to precise measurements of  $\lambda$  for many planetary systems to determine the fraction of planets among the exoplanet population with a significant inclination. Measurements

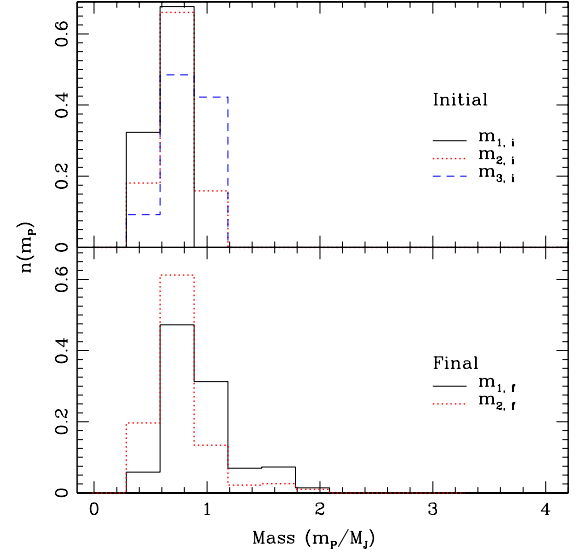


FIG. 14.— Initial and final mass distributions of the closest, middle and furthest planets. The top (bottom) panel shows the initial (final) mass distributions. Solid (black), dotted (red), and dashed (blue) lines in the top panel represent the initial mass histograms of the closest, middle, and furthest planets. Solid (black) and dotted (red) lines in the bottom panel represent the mass histograms of the final inner and outer planets, respectively. One planet is ejected in each of our simulations. Note that the histogram for the inner planet masses shifts towards higher values in the bottom panel, which indicates that the higher mass planets preferentially become the inner planet in the final stable configuration of the planetary systems.

of  $\lambda$  would be particularly interesting for the massive short-period planets ( $m > M_J$ ) or for very-short period giant planets ( $P < 2.5$  d), since these planets might have a different formation history than the short-period planets with  $m \simeq 0.5M_J$  that are more common.

Our simulations show the effects of mass segregation, as heavier planets preferentially end with smaller semi-major axes. This trend can be easily seen by comparing the initial and final mass distributions of the planets in Figure 14. The mass distribution clearly shifts towards higher mass values in the final inner planet mass histogram whereas the outer planet mass essentially reflects the initial mass distribution (compare the top and bottom panels of Figure 14).

We do not find a strong effect of mass on eccentricity but we note that collisions tend to reduce the fraction of highly eccentric systems (Figure 15). The collision products can be seen in the cluster around and above  $1.5 M_J$ . We find no other significant mass dependent effect in the final orbital parameters.

#### 3.4. Mean Motion Resonances

In the radial-velocity planet population there are 172 planetary systems with 200 planets. These include 20 multi-planet systems and at least 5 systems that include a MMR (4 appear to be in 2:1 MMR). MMRs can have strong effects on the dynamical evolution and stability of those planetary systems. The 2:1 MMR is particularly interesting due to the proximity of the two orbits and the increased possibility for close encounters that could result in strong gravitational scattering between the two planets (Sándor & Kley 2006).

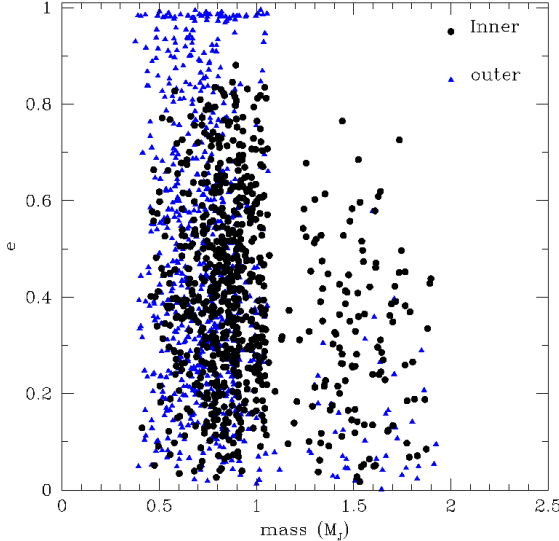


FIG. 15.— Mass vs eccentricity of the final stable planets. The circles (black) and the triangles (blue) represent the final inner and the outer planets. Planets with masses  $\geq 1.6 M_J$  are collision products. The collision planets tend to have lower eccentricities.

It is widely believed that MMRs between two or more planets in a planetary system arise naturally from migration. Convergent migration in a dissipative disk can lead to resonant capture into a stable MMR, particularly the 2:1 MMR (Lee & Peale 2002).

While we regard differential migration as a natural way to trap two planets into MMRs, here we explore the possibility of trapping two planets into MMR using only their mutual gravitational perturbations and without any damping. In a 3-planet system it is possible that one planet can act as a source or sink of energy to let the other two planets dynamically evolve into or out of a MMR. If pure dynamical trapping into MMRs were efficient, then this would open up interesting possibilities. For one, it does not require a common disk origin, as is a requirement for the migratory origin of MMR. Additionally, this mechanism could operate in a planetary system at a much later time after the protoplanetary disk has been depleted.

To look for possible 2:1 MMR candidates, we isolate the systems that have two planets with their final periods in close to 2:1 ratios. First, we choose systems where the final ratio of periods is between 1.8 – 2.2. Then we calculate the two resonance angles  $\theta_1$  and  $\theta_2$  over the full time of their dynamical evolution. Here the two resonance angles are given by

$$\theta_{1,2} = \lambda_1 - 2\lambda_2 + \varpi_{1,2}, \quad (14)$$

where  $\lambda_1$  and  $\lambda_2$  are the mean longitudes of the inner and outer planets and  $\varpi_1$  and  $\varpi_2$  are the longitudes of periastron for the inner and outer planets. When the planets are not in a MMR,  $\theta_{1,2}$  circulate through  $2\pi$ . When trapped in a MMR, the angles librate around two values (Lee 2004). Finally, we check whether the periodic ratio and libration of the resonant angles are long lived or just a transient stage in their dynamical evolution.

We find one system where two planets are caught into a 2:1 MMR (Fig. 16). The top two panels show the time evolution of the resonant arguments  $\theta_1$  and  $\theta_2$ . Note

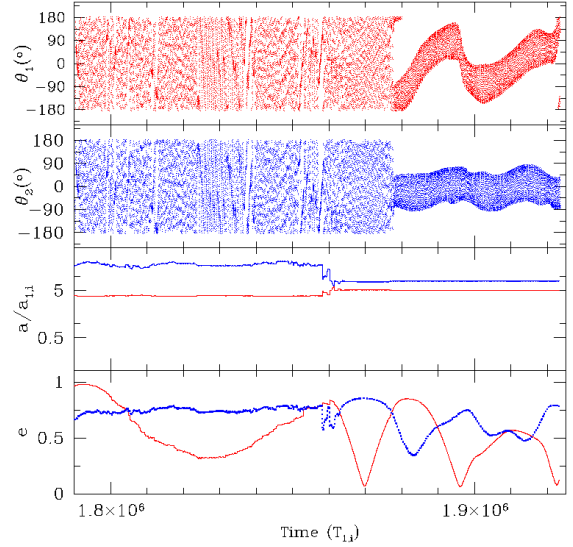


FIG. 16.— Time evolution plots for the two resonance angles  $\theta_1$  and  $\theta_2$ , the semi-major axes and the eccentricities of the planets. From top to bottom the panels show the time evolutions of  $\theta_1$ ,  $\theta_2$ , semi-major axes and eccentricities, respectively. The time axis is in units of the initial orbital period of the initially closest planet ( $T_{1,i}$ ). For the panels showing semi-major axes and eccentricity, the solid (red) and dotted (blue) lines show the evolutions of the two planets that enter a 2:1 MMR. Note that a little before  $1.88 \times 10^6 T_{1,i}$  both  $\theta_1$  and  $\theta_2$  start librating.

how the two angles go from the circulating phase to the librating phase at around  $1.88 \times 10^6 T_{1,i}$ . The two bottom panels show the time evolution of the semi-major axes and the eccentricities of the two planets in MMR. Note that the semi-major axes are nearly constant and the eccentricities oscillate stably. Since there is no damping in the system, the somewhat large libration amplitude of the resonant angles is to be expected. In principle, the presence of even a little damping (due to some residual gas or dust in the disk) might reduce the amplitudes of libration and eccentricity oscillations for systems such as this one.

It is important to note that systems like the one illustrated in Figure 16 are not a typical outcome of our simulated population. We find that it is improbable to trap two planets in a 2:1 MMR only through dynamics for a long period of time when no damping is present. We find a few ( $\sim 1\%$ ) other systems showing similar librations of  $\theta_{1,2}$  at different times during their dynamical evolution, but for them the libration phase is shorter, never being more than a few times  $10^3 T_{1,i}$ . However, if our simulations were to include some dissipation, then the frequency of such systems might be increased significantly. We encourage future investigations of this possibility.

### 3.5. A different mass distribution

To test the sensitivity of our results to the choice of mass distribution, we perform the same study as before with a different mass distribution (we call this mass distribution 2 henceforth). The numerical setup is exactly the same as described in Sec. 3.1 but the masses of the cores are assigned differently. Here we assign the planetary core masses  $M_{core}$  from a distribution of masses between  $1 - 100 M_\oplus$  uniform in  $M_{core}^{1/5}$  and assume that

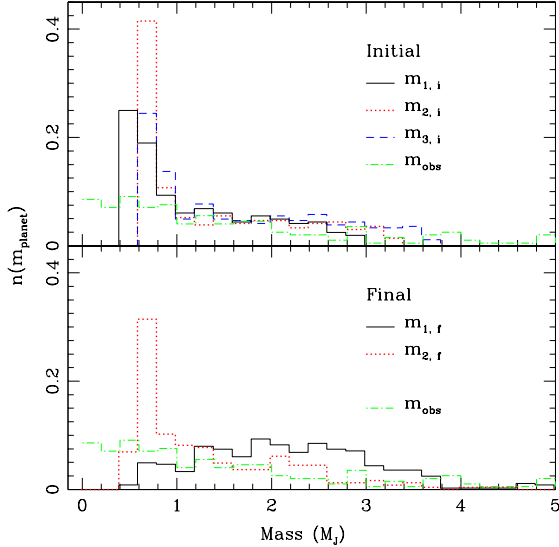


FIG. 17.— Same as Figure 14, but with a different and wider initial mass distribution than the previous one. The initial mass distribution has a high number of Jovian mass planets as in the previous mass distribution, however, in this case the distribution has a tail towards higher masses. The higher end in the initial mass spectra in this case mimic the minimum mass ( $m \sin i$ ) spectrum of the observed exoplanets. Note that the mass segregation effect is more prominent here than in Figure 14. The dot-dash (green) line shows the  $m \sin i$  distribution of the observed exoplanets in both panels for comparison.

the cores accrete all the gas within 10 Hill radii of them. The exponent in the core mass distribution and the surface density at 1 AU,  $\Sigma_1$ , are chosen somewhat arbitrarily with the goal to obtain an initial mass distribution that has a large number of Jupiter mass ( $M_J$ ) planets and a few higher mass planets with the number density going down with increasing mass (Fig. 17). The number density of the higher mass planets mimics the mass distribution of the observed exoplanets. Our sample size here is 500. The above mentioned choices produce initial masses of the planets in the range  $0.4 M_J - 4 M_J$ .

This choice of mass distribution also enables us to observe mass dependent effects more clearly. For example, we see that the higher mass planets preferentially become the final inner planets (Figure 17) more prominently. The cumulative distributions of the eccentricities compare better with the observed eccentricities (Figure 18) for mass distribution 2. We do not find the very highly eccentric ( $e > 0.8$ ) planetary orbits in this case as in the case of mass distribution 1. The final semi-major axis distribution is statistically indistinguishable from the semi-major axis distribution resulting from mass distribution 1. Semi-major axis and eccentricity have a weak anti-correlation (Figure 19). We do not find any systems with two planets trapped in 2:1 MMR for this case. Even transient libration of the arguments as in mass distribution 1 for some planetary systems is absent in our sample for mass distribution 2.

#### 4. SUMMARY AND CONCLUSIONS

We have studied in detail how the orbital properties change due to strong gravitational scattering between multiple giant planets in a planetary system containing three giant planets around a solar mass star. We characterize the stability of a planetary system depending

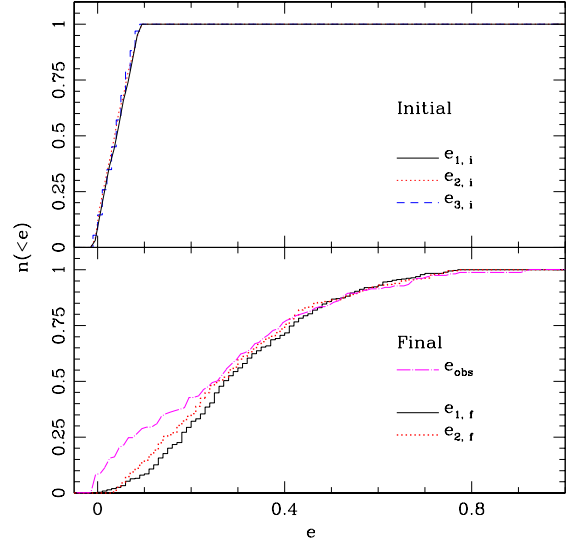


FIG. 18.— Same as Figure 7, but using mass distribution 2. The solid (black) line, and the dotted (red) lines in the bottom panel show the eccentricity distributions of the final inner and outer planets in the simulated population. The dash-dot (magenta) line show that of the observed exoplanet population with mass  $\geq 0.4 M_J$ . The simulated and observed eccentricities match much better in this case, particularly for  $e \geq 0.2$ .

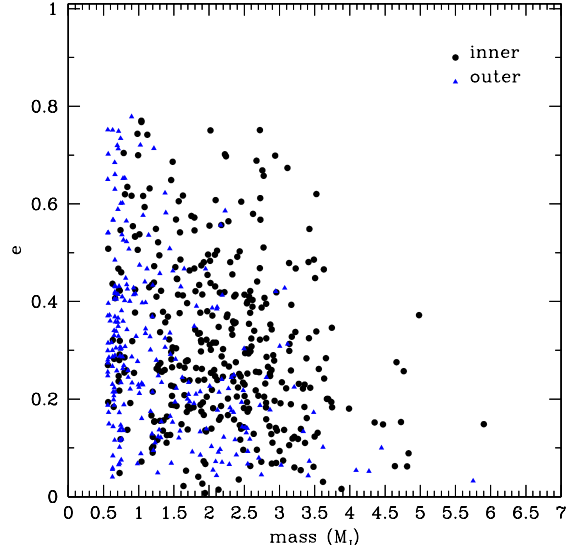


FIG. 19.— Same as Figure 15, but using the broader distribution of initial planet masses. There seems to be a weak anti-correlation between the mass and the eccentricities of the planets.

on the initial separation between the planets given in units of their mutual Hill radii (Figure 2). Stability of planetary systems increases quickly with the increasing  $K$  value. We recognize resonance signatures as dips and rises in the stability timescale. We show that the timescale distributions of these systems, initially near and away from major MMR are qualitatively different (Figure 4), whereas two different  $K$  values both away from MMR show the same qualitative shape in the stability time distribution (Figure 3). This observation bolsters our belief that the final outcomes of the numerical simulations do not differ qualitatively if  $K$  is changed as long as the chosen value of  $K$  ensures that the plane-

tary system is not near a major MMR initially. A higher or lower  $K$  value satisfying the above requirement will increase or decrease the timescale until instability of the planetary systems, but not qualitatively change the outcomes following one or more strong scattering phases. One notable exception is that for very low  $K$ , collisions between the planets can become more frequent due to gravitational focusing.

We study the final orbital properties of the planets that remain bound to the central star in stable orbits after chaotic evolution due to strong mutual interactions. We perform the experiments with realistic planetary systems containing 3 giant planets (cf. Sec. 3.1). In all of our simulated systems at least one planet is eventually ejected before reaching a stable configuration. This supports models of planet formation that initially form planetary systems overstuffed with planets and instabilities reduce the number of planets until the timescale for instability exceeds the age of the planetary system. In 20% of the cases, two planets are ejected leaving the system with only one giant planet. Thus, the planet scattering model predicts the existence of many systems with a single eccentric giant planet, as well as many free floating planets. We find that strong gravitational scattering between giant planets can naturally create high eccentricity orbits. Although our first set of models predicts eccentric planets to be slightly more common than observed (Figure 7), a wider initial mass distribution can result in remarkable similarity with the observed distribution (Figure 18). We conclude that planet–planet scattering can easily account for the observed distribution of eccentricities ranging from 0.2–0.8. Our simulations under-produce systems with eccentricities less than 0.2. This may suggest that some observed systems are affected by late stage giant collisions. Alternatively, the presence of some damping from a gas or planetesimal disk could lead to eccentricity damping. We find this latter explanation particularly attractive due to the observed correlation between planet mass and eccentricity (Butler et al. 2006). While our simulations find that high eccentricities are most common among less massive giant planets, the known population of extrasolar planets suggest that high eccentricities are more common among the more massive planets (Ford & Rasio 2007). This apparent discrepancy could be resolved if a modest disk often remains after the final major planet–planet scattering event. Less massive planets would be more strongly affected by the remaining disk, so their eccentricities could be damped, while more massive planets would typically be immune to eccentricity damping.

We also find that it is possible to scatter some planets at highly inclined orbits with low perihelion distances (Figure 9). Approximately 10% of the systems obtain perihelion distances less than  $0.1 a_{i,1}$ . If the initial semi-major axes are small enough, then it is possible for strong gravitational scattering to result in planet orbits with sufficiently small perihelion distances, which tidal effects will circularize to create hot Jupiters.

If we assume that the angular momentum of the host star is aligned with that of the orbital angular momentum of the planets, then measurements of  $\lambda$  should typically

be small in the absence of perturbations from other planetary or stellar companions (cf. Sec. 3.3). We find that strong gravitational scattering between the giant planets can naturally increase the inclinations of the final planetary orbits with respect to the initial total orbital angular momentum plane (Figure 11). Since the timescale to tidally align the stellar spin and the planetary angular momentum is much greater than the age of the star ( $\sim 10^{12}$  years) (Greenberg 1974; Hut 1980; Winn et al. 2005), inclinations excited by planet–planet scattering after the disk had dispersed could be maintained for the entire stellar lifetime. Observations of a hot-Jupiter with a significantly non-zero  $\lambda$  would be suggestive of previous planet–planet scattering. However, caution would be necessary if the star had a binary stellar companion (Wu & Murray 2003; Takeda & Rasio 2005, Fabrycky 2007). On the other hand, observations of many hot-Jupiters with orbital angular momenta closely aligned with their stellar rotation axis would suggest a formation mechanism other than strong gravitational scattering followed by tidal circularization. Unfortunately, current observations only measure this angle for a few systems and have uncertainties comparable to the dispersion of inclinations found in our simulations. We encourage observers to improve both the number and precision of Rossiter–McLaughlin observations.

Although effects of a debris disk on planetary dynamics and vice versa is not within the scope of this study, the warped disk observed in  $\beta$  Pictoris could be one interesting example where inclined planetary orbits and the debris disk exchange torques, resulting in a warped debris disk (Smith & Terrile 1984; Heap et al. 2000). Mouillet et al. (1997) suggests that the observed asymmetry in the debris disk can be explained by the presence of a planetary companion in an inclined orbit. Strong planetary scattering, as we find, can be a natural way to create planetary orbits inclined to the initial invariable plane.

We find that a few percent of the simulated population have very high semi-major axes in the final stable configuration. Strong planet–planet scattering can be one natural way to form distant ( $a > 50$  AU) giant planets from the star (Veras & Armitage 2004). Such giant planets are extremely unlikely to be created *in situ*, since the timescale for planet formation greatly exceeds the age of the star. Additionally, there is simply insufficient disk mass to form a giant planet at such large orbital distances (Kokubo & Ida 2002; Ida & Lin 2004b,a). Strong scattering between planets in multi-planet systems can be a natural mechanism to create such long-period planets. We find that this population of high semi-major axis planets will have high eccentricities and inclinations (Fig. 8). Future planet searches using astrometry or direct detection can test these predictions.

This work was supported by NSF grants AST-0206182 and AST-0507727 at Northwestern University. Support for E.B.F. was provided by NASA through Hubble Fellowship grant HST-HF-01195.01A awarded by the Space Telescope Science Institute, which is operated by the Association of Universities for Research in Astronomy, Inc., for NASA, under contract NAS 5-26555.

## REFERENCES

Black, D. C. 1997, ApJ, 490, 171

Butler, R. P., Wright, J. T., Marcy, G. W., Fischer, D. A., Vogt, S. S., Tinney, C. G., Jones, H. R. A., Carter, B. D., Johnson, J. A., McCarthy, C., & Penny, A. J. 2006, ApJ, 646, 505

Chambers, J. E. 1999, MNRAS, 304, 793

Chambers, J. E., Wetherill, G. W., & Boss, A. P. 1996, Icarus, 119, 261

Faber, J. A., Rasio, F. A., & Willem, B. 2005, Icarus, 175, 248

Ford, E. B., Havlickova, M., & Rasio, F. A. 2001, Icarus, 150, 303

Ford, E. B. & Rasio, F. A. 2006, ApJ, 638, L45

Ford, E. B., Rasio, F. A., & Yu, K. 2003, in ASP Conf. Ser. 294: Scientific Frontiers in Research on Extrasolar Planets, ed. D. Deming & S. Seager, 181–188

Gladman, B. 1993, Icarus, 106, 247

Goldreich, P., Lithwick, Y., & Sari, R. 2004, ApJ, 614, 497

Greenberg, R. 1974, Icarus, 23, 51

Heap, S. R., Lindler, D. J., Lanz, T. M., Cornett, R. H., Hubeny, I., Maran, S. P., & Woodgate, B. 2000, ApJ, 539, 435

Holman, M., Touma, J., & Tremaine, S. 1997, Nature, 386, 254

Hut, P. 1980, A&A, 92, 167

Ida, S. & Lin, D. N. C. 2004a, ApJ, 604, 388

—. 2004b, ApJ, 616, 567

Kokubo, E. & Ida, S. 1998, Icarus, 131, 171

—. 2002, ApJ, 581, 666

Lee, M. H. 2004, ApJ, 611, 517

Lee, M. H. & Peale, S. J. 2002, ApJ, 567, 596

Lin, D. N. C. & Ida, S. 1997, ApJ, 477, 781

Lissauer, J. J. 1995, Icarus, 114, 217

Marzari, F. & Weidenschilling, S. J. 2002, Icarus, 156, 570

Mazeh, T., Krymolowski, Y., & Rosenfeld, G. 1997, ApJ, 477, L103

Mouillet, D., Larwood, J. D., Papaloizou, J. C. B., & Lagrange, A. M. 1997, MNRAS, 292, 896

Papaloizou, J. C. B. & Terquem, C. 2001, MNRAS, 325, 221

Rasio, F. A. & Ford, E. B. 1996, Science, 274, 954

Sándor, Z. & Kley, W. 2006, A&A, 451, L31

Smith, B. A. & Terrile, R. J. 1984, Science, 226, 1421

Takeda, G. & Rasio, F. A. 2005, ApJ, 627, 1001

Terquem, C. & Papaloizou, J. C. B. 2002, MNRAS, 332, L39

Tremaine, S. & Zakamska, N. L. 2004, in AIP Conf. Proc. 713: The Search for Other Worlds, ed. S. S. Holt & D. Deming, 243–252

Veras, D. & Armitage, P. J. 2004, MNRAS, 347, 613

Weidenschilling, S. J. & Marzari, F. 1996, Nature, 384, 619

Winn, J. N., Johnson, J. A., Marcy, G. W., Butler, R. P., Vogt, S. S., Henry, G. W., Roussanova, A., Holman, M. J., Enya, K., Narita, N., Suto, Y., & Turner, E. L. 2006, ApJ, 653, L69

Winn, J. N., Noyes, R. W., Holman, M. J., Charbonneau, D., Ohta, Y., Taruya, A., Suto, Y., Narita, N., Turner, E. L., Johnson, J. A., Marcy, G. W., Butler, R. P., & Vogt, S. S. 2005, ApJ, 631, 1215

Wu, Y. & Murray, N. 2003, ApJ, 589, 605

Zakamska, N. L. & Tremaine, S. 2004, AJ, 128, 869